

Article

Crystallization Kinetics and Consolidation of $\text{Al}_{82}\text{La}_{10}\text{Fe}_4\text{Ni}_4$ Glassy Alloy Powder by Spark Plasma Sintering

Nguyen Hoang Viet ¹, Nguyen Thi Hoang Oanh ^{1,*}, Ji-Soon Kim ² and Alberto Moreira Jorge Jr. ^{3,4,5,6,7}

¹ School of Materials Science and Engineering, Hanoi University of Science and Technology, Hanoi 100000, Vietnam; viet.nguyenhoang@hust.edu.vn

² School of Materials Science and Engineering, University of Ulsan, 55-12, Technosanup-ro, Nam-Gu, Ulsan 44776, Korea; jskim@ulsan.ac.kr

³ Department of Materials Science and Engineering, Federal University of São Carlos, Via Washington Luiz, km 235, São Carlos, SP 13565-905, Brazil; moreira@ufscar.br

⁴ University of Grenoble Alpes, Science et Ingénierie des Matériaux et Procédés (SIMAP), F-38000 Grenoble, France

⁵ Centre National de la Recherche Scientifique (CNRS), Science et Ingénierie des Matériaux et Procédés (SIMAP), F-38000 Grenoble, France

⁶ University of Grenoble Alpes, Laboratoire d'Electrochimie et de Physico-chimie des Matériaux et des Interfaces (LEPMI), F-38000 Grenoble, France

⁷ Centre National de la Recherche Scientifique (CNRS), Laboratoire d'Electrochimie et de Physico-chimie des Matériaux et des Interfaces (LEPMI), F-38000 Grenoble, France

* Correspondence: oanh.nguyenthihoang@hust.edu.vn; Tel.: +84-93-6029-098

Received: 15 September 2018; Accepted: 8 October 2018; Published: 11 October 2018



Abstract: The mechanically alloyed $\text{Al}_{82}\text{La}_{10}\text{Ni}_4\text{Fe}_4$ glassy powder displays a two-step devitrification characterized by the precipitation of fcc-Al together with small amounts of the intermetallic $\text{Al}_{11}\text{La}_3$ phase in the first crystallization. The interface-controlled growth mechanism governed the first crystallization event. Calculations of the activation energy, using the methods of Kissinger, Ozawa, and Augis-Bennett gave values of 432.33, 443.2, and 437.76 kJ/mol, respectively. The calculated Avrami exponent (n) for the first crystallization peak was about 1.41, suggesting an almost zero nucleation rate. On the other hand, the value of n for the second peak related to the residual amorphous phase completely transformed into the intermetallic phase $\text{Al}_{11}\text{La}_3$ was about 3.61, characterizing diffusion controlled three-dimensional crystal growth with an increasing nucleation rate. Samples sintered at 573 K kept an amorphous structure and exhibited a high compressive strength of 650 MPa with a maximum elongation of 2.34% without any plastic deformation. The failure morphology of the sintered sample surface presented a transparticle fracture mechanism, indicating the efficiency of the sintering processing.

Keywords: bulk amorphous alloys; mechanical alloying; spark plasma sintering; crystallization kinetics; Avrami exponent

1. Introduction

To date, several multicomponent bulk metallic glasses (BMGs) with outstanding mechanical, as well as corrosion properties, have been developed. Among these novel materials, Al-RE (La, Y, Ce)-TM (Fe, Co, Ni) alloys [1–4] have been found to exhibit a particularly valuable combination of high strength and low density, which make them viable candidates for engineering applications, especially

for the aerospace industry [5]. Scudino et al. reported a bulk $\text{Al}_{87}\text{Ni}_8\text{La}_5$ alloy was prepared by spark plasma sintering (SPS) of gas atomized powders exhibits a high compression strength of 930 MPa with a multiphase structure consisting of fcc-Al, $\text{Al}_{11}\text{La}_3$ and Al_3Ni phases [4]. Fracture strength of about 1260 MPa has been reported for an amorphous $\text{Al}_{85}\text{Y}_5\text{Ni}_7\text{Co}_3$ alloy [6] that is more than twice the one for ordinary Al alloys. Mechanical resistance of some Al-RE-TM alloys may be enhanced by partial crystallization, where nanoscale fcc-Al precipitates are uniformly distributed in the amorphous matrix [7–10].

Metallic glasses are amid the most enthusiastically studied metallic materials. Whichever has thin ribbons or bulk pieces, they are bringing up several new and applicable properties, running very well inside the mechanical, physical, and chemical domains [11–15]. The fundamental knowledge of glass forming ability (GFA) in multicomponent alloys is based on some criteria (summarized by Suryanarayana and Inoue [15]) to select compositions that could improve GFA.

Either by direct melt cooling or through solid-state amorphization techniques, a huge number of glass-forming alloys have been produced from binary to multicomponent alloy systems since its viability demonstration came in 1959 [16]. However, so far, only a few multicomponent alloys [17–19] are likely to be cast at relatively low cooling rates into the large thickness glassy state pieces, the bulk metallic glass (BMG). In these alloys, instead of the cooling rate, as it is the case for ordinary metallic glasses, the critical condition for glass formation is the undercooling level [16,20]. Combined to the ease of viscous flow, this should enable near net shape processes to be used for producing exceptional technological components. BMG alloys produced by rapid solidification techniques are size limited (from few millimeters to few centimeters) due to the critical cooling rate necessary for lengthening the time the molten metal staying in the supercooled state, thus restricting their potential application fields [21,22].

Powder metallurgy (PM) methods, such as mechanical alloying (MA) followed by SPS, have been used to produce bulk Al-based alloys. MA is the most popular to synthesize amorphous alloy powders [23,24]. Generally, there are no so many studies performed systematically to recognize factors that may contribute to the formation of an amorphous phase by MA. Probably, one may say that such lack of research is due to MA, which is a complicated process and comprises several processing parameters, including, amongst others, composition, particle size, type of mill machine and milling means, ball-to-powder weight ratio, time, temperature, milling environment, type and quantity of the agent controlling the process. As a consequence, there are solely some studies regarding parameters that can describe the GFA, which are related to the total energy, impact energy, power absorption, and ball-to-powder weight ratio [15]. The greatest advantage of MA in the synthesis of BMG alloys is that powders may be produced in the amorphous state and are subsequently consolidated in the supercooled liquid region to any section thickness [25,26]. The properties of the liquid defining the GFA of the alloy is not restricted to deep eutectics in the phase diagram, as is frequently the case for melt spinning, but wide glass-forming ranges exist in the central composition range in alloys proceeded by MA [27]. The SPS is a highly effective method to densify hard-to-sinter materials in a rather short time at much lower sintering temperatures than those required in conventional consolidation processes. Numerous experimental and theoretical investigations on the process suggest the ability of SPS to provide highly dense compacted powder products with the potential of retaining amorphous structure [28,29]. Specifically, in the case of Al-RE (La, Y, Ce)-TM (Fe, Co, Ni), several works have been reported in the literature on SPS consolidation (see for instance [30–32] and references therein). However, even potentially maintaining the amorphous state, the risk of a possible crystallization during high-temperature exposure continues to be the most significant problem of the consolidation of glassy powders. Therefore, to take advantage of the PM approach for fabricating bulks from Al-based amorphous powder, an in-depth study of the crystallization kinetics of such powders is necessary. Crystallization studies of amorphous alloys play a fundamental role in the area of amorphous and nanostructured alloys. The control of the microstructure evolution of glassy precursors requires a detailed understanding of specific mechanisms influencing the structural transformation [30].

Moreover, crystallization studies are essential for the proper choice of specific consolidation parameters (i.e., time and temperature) to maximize the densification, and at the same time, retaining the amorphous structure [33,34]. However, detailed information on the crystallization kinetics of the ball-milled $\text{Al}_{82}\text{La}_{10}\text{Ni}_4\text{Fe}_4$ alloy has not been obtained yet and needs a deep investigation.

In this study, besides complete characterization of $\text{Al}_{82}\text{La}_{10}\text{Ni}_4\text{Fe}_4$ amorphous powders produced by ball milling, the crystallization kinetics of such mechanically alloyed powders has been investigated using differential scanning calorimetry (DSC) in the non-isothermal mode using several techniques of analysis. In addition, the study of SPS consolidated amorphous powders for preparing bulk amorphous samples at different temperatures was also performed, among them is densification tests and mechanical behavior of consolidated specimens, which were evaluated by micro-hardness and compression tests followed by failure analysis.

2. Materials and Methods

Pure powders of Al (purity $\geq 99.7\%$, $-100 + 325$ mesh, CERACTM, Milwaukee, WI, USA), Fe (purity $\geq 99.5\%$, Junsei Chemical Co., Ltd., Tokyo, Japan), Ni (purity $\geq 99.99\%$, -100 mesh, Aldrich Chem. Co, Inc., Milwaukee, WI, USA) and La (purity $\geq 99.9\%$, 40 mesh, CERACTM) were mixed with the desired nominal composition of $\text{Al}_{82}\text{La}_{10}\text{Fe}_4\text{Ni}_4$ and loaded into stainless steel vials with stainless steel balls. The powder to ball weight ratio was 1:20. The vials were evacuated and filled with the protective Ar gas, under a pressure of 3×10^5 Pa. Mechanical alloying was performed with a high-energy planetary ball-mill (AGO-2) at a rotational speed of 300 rpm, where the vials were water-cooled. Without using a process control agent (PCA), there was a substantial agglomeration of powders and their sticking on the milling tools. Therefore, milling was carried out with an addition of 50 mL hexane as PCA. After milling, powders were dried in a vacuum furnace at 353 K to vaporize hexane in as-milled powders.

Particle size distribution of the sample was measured using a Malvern Panalytical's Mastersizer 2000 laser diffractometer (Malvern Panalytical, Malvern, UK). The thermal stability of amorphous powders was studied by differential scanning calorimetry (DSC) in a non-isothermal mode with a NETZSCH STA 409C under a continuous flow of purified argon gas. The non-isothermal DSC studies were carried out at different heating rates of 5, 10, 20, and 40 K/min.

The consolidation of amorphous powders was performed by spark plasma sintering (SPS), using a pulsed current using the SPS-515 Sumitomo Coal Mining spark plasma sintering equipment (Sumitomo Coal Mining Co., Ltd., Tokyo, Japan). The chamber was evacuated to a pressure <5 Pa. The mold and punches (10 mm diameter) are made of the WC-Co alloy. An amount of 1.5 g of amorphous powders were spark plasma sintered at various sintering temperatures from 543 to 623 K, at a heating rate of 10 K/min and applied pressures of 500 MPa during 3 min of holding time.

Phase analysis was performed by X-ray diffraction (XRD) in a SIEMENS D5000 diffractometer (Siemens, Berlin, Germany) using Cu $K\alpha$ radiation ($\lambda = 1.5405 \text{ \AA}$). The XRD parameters were: 2θ range of 20 to 80° , a step size of 0.03° , scanning speed 1° per min. The morphology of the powders and fracture analyses of bulk samples were characterized by field-emission scanning electron microscopy (FE-SEM) using a JEOL JSM-7600F (JEOL Ltd., Tokyo, Japan). SPS samples were mechanically polished using coarse and fine grinding by abrasive papers and finally fine polishing by using Al_2O_3 powder. Pore distribution on the surface and relative densities of bulk samples was performed by Olympus PMG3 optical microscope (Olympus Corporation, Tokyo, Japan) with computerized image analysis with a magnification of $100\times$. Density of bulk composites was determined by Archimedes method. Vickers microhardness measurements were performed using a Mitutoyo MVK-H1 Hardness Testing Machine (Mitutoyo Corporation, Kanagawa, Japan) under a load of 100 g. Compression tests of sintered samples were performed with a normal displacement rate of 0.1 mm/min in an Instron 4469 Advanced Tensile Tester (Instron[®], Norwood, CO, USA).

Possible contamination by carbon and oxygen after long milling time was determined by inductively coupled plasma (ICP) spectroscopy (Varian, Vista-Megapixel MPX, Mulgrave, Australia). Such measurements gave values of 3.3 ± 0.7 at. % for carbon and less than 100 ppm for oxygen.

3. Results and Discussion

3.1. Crystallization Kinetics

Figure 1 shows an X-ray diffraction pattern of the $\text{Al}_{82}\text{La}_{10}\text{Fe}_4\text{Ni}_4$ amorphous powder alloy after MA during 350 h. The XRD trace shows a broad diffuse diffraction peak at about 36 degrees, characterizing an X-ray amorphous structure.

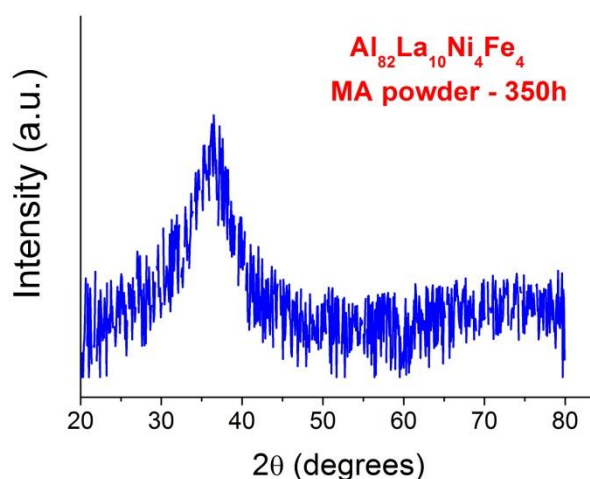


Figure 1. XRD (X-ray diffraction) pattern of the mechanically alloyed $\text{Al}_{82}\text{La}_{10}\text{Fe}_4\text{Ni}_4$ powder.

Figure 2a presents a SEM observation of the as-milled $\text{Al}_{82}\text{La}_{10}\text{Fe}_4\text{Ni}_4$ amorphous powder, where it can be seen agglomerates of fine powder particles whose sizes are far below $15 \mu\text{m}$. The particle shape appears to be more spherical than flake-like, indicating that sliding events dominated during ball-collisions. Particle size distribution of the sample is shown in Figure 2b, where it is possible to observe a unimodal distribution. Measurements gave an average particle size ($d_{0.5}$) of about $14.42 \mu\text{m}$.

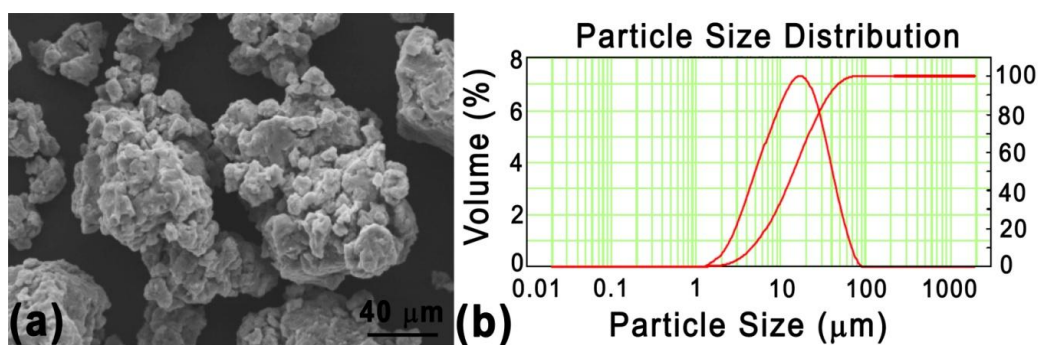


Figure 2. (a) FE-SEM (field-emission scanning electron microscopy) image and (b) particle size distribution of $\text{Al}_{82}\text{La}_{10}\text{Fe}_4\text{Ni}_4$ amorphous powder.

Figure 3 presents DSC scans at different heating rates (β) for the as-milled $\text{Al}_{82}\text{La}_{10}\text{Fe}_4\text{Ni}_4$ amorphous powders. DSCs show two large exothermic events, probably indicating two-step crystallization. Before the first peak, every DSC curve exhibits a small endothermic event, thermally manifesting a slight rise in specific heat (C_p) and characterizing a glass transition temperature (T_g), whose values are roughly indicated in the figure. The two exothermic peaks are characteristically determined by onset (T_{x1} and T_{x2}) and peak (T_{p1} and T_{p2}) temperatures. Table 1 summarizes values of

T_x and T_p , as well as the supercooled liquid region value ($\Delta T_x = T_{x1} - T_g$), at different heating rates. As expected, the characteristic temperatures shift towards higher temperatures as the heating rate is increased from 5 to 40 K/min. The super-cooled liquid region is similar for all the conditions having an average value of about 24 K.

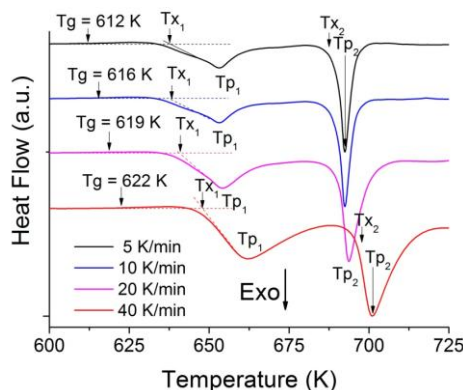


Figure 3. DSC (differential scanning calorimetry) curves of $\text{Al}_{82}\text{La}_{10}\text{Fe}_4\text{Ni}_4$ amorphous powder at various heating rates.

Table 1. Thermal parameters of the amorphous $\text{Al}_{82}\text{La}_{10}\text{Fe}_4\text{Ni}_4$ alloy at different heating rates.

Heating Rate β , K/min	ΔT_x (K)	T_{x1} (K)	T_{p1} (K)	T_{x2} (K)	T_{p2} (K)
5	24.3	636.6	651.6	686.2	689.3
10	23.5	638.9	652.6	690.5	693.0
20	23.1	641.1	653.7	690.8	694.3
40	24.1	648.2	662	695.6	701.0

To study structural changes of the $\text{Al}_{82}\text{La}_{10}\text{Fe}_4\text{Ni}_4$ amorphous powders during heating, they were annealed in the DSC under continuous heating at 40 K/min up to different temperatures throughout exothermic peaks and then cooled down to room temperature at 100 K/min. Figure 4 presents XRD patterns of crystallized samples in comparison with the amorphous one. Figure 4b displays the result after heating the sample up to the completion of the first exothermic DSC peak (at 682 K). As one can observe, both the fcc-Al and the intermetallic phase $\text{Al}_{11}\text{La}_3$ have precipitated, and are superimposed to a small amorphous halo. Indeed, due to the very small amount of the intermetallic phase, this result indicates that the first crystallization is composed by nanocrystals of fcc-Al. After annealing at 758 K, full crystallization occurs (Figure 4c). In this case, only the intermetallic phase $\text{Al}_{11}\text{La}_3$ is present and fcc-Al is entirely transformed in $\text{Al}_{11}\text{La}_3$. No other phase is observed at any annealing temperature, which may be due to the minimal amount of Fe and Ni elements. In this way, it is believed that the large second exothermic peak in Figure 3 is due to phase transformation from fcc-Al to $\text{Al}_{11}\text{La}_3$.

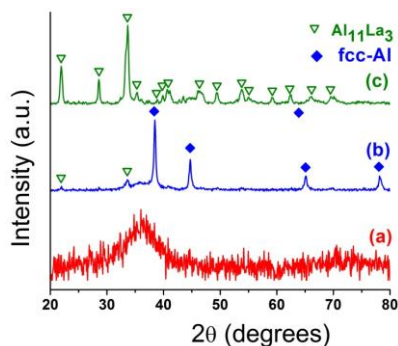


Figure 4. XRD trace of amorphous $\text{Al}_{82}\text{La}_{10}\text{Fe}_4\text{Ni}_4$ MA powder: (a) as-milled powder and heat treatment for (b) first and (c) second crystallization peak temperatures of 682 and 758 K, respectively.

The activation energy (E_a) for the crystallization process gives valuable information regarding the thermal stability of the sample. Such activation energy can be evaluated from constant-rate heating DSC curves taken at different heating rates using the Kissinger, Ozawa, and Augis-Bennett equations, as given by Equations (1)–(3), respectively: [35,36]

$$\ln\left(\frac{\beta}{T_p^2}\right) = -\frac{E_a}{RT_p} + \text{const} \quad (1)$$

$$\ln(\beta) = -\frac{E_a}{RT_p} + \text{const} \quad (2)$$

$$\ln\left(\frac{\beta}{T_p - T_0}\right) = -\frac{E_a}{RT_p} + \text{const} \quad (3)$$

where β is the heating rate, T_p is the temperature at the exothermal peak, R is the gas constant, and E_a is the activation energy of crystallization. Figure 5a–c show the Kissinger plot $\ln(\beta/T_p^2)$ versus $1000/T_p$, Ozawa plot $\ln(\beta)$ versus $1000/T_p$, Augis-Bennett plot $\ln(\beta/T_p - T_0)$ versus $1000/T_p$, respectively. All plots yield straight lines with a good fit.

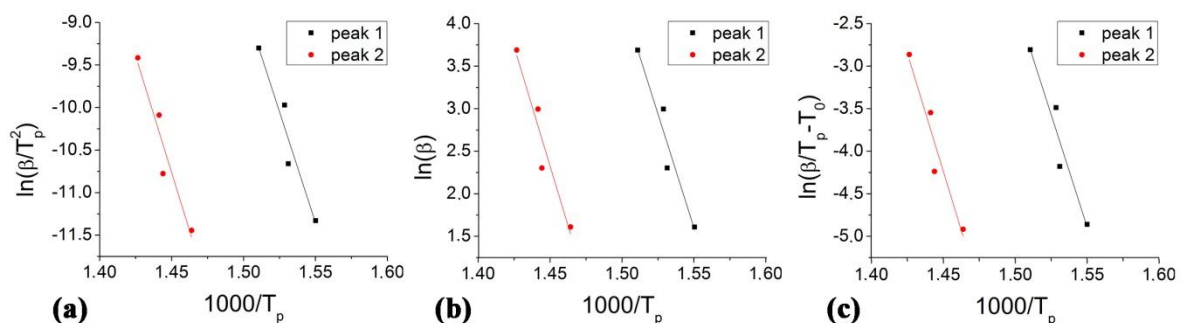


Figure 5. (a) Kissinger plot of the $\text{Al}_{82}\text{La}_{10}\text{Fe}_4\text{Ni}_4$ amorphous powder. (b) Ozawa plot of the $\text{Al}_{82}\text{La}_{10}\text{Fe}_4\text{Ni}_4$ amorphous powder. (c) Augis-Bennett plot of the $\text{Al}_{82}\text{La}_{10}\text{Fe}_4\text{Ni}_4$ amorphous powder.

The Avrami exponent (n) gives detailed information on the nucleation and growth mechanism of new crystalline grains during the phase transition, which can be obtained by Johnson-Mehl-Avrami (JMA) equation [37,38]:

$$x(t) = 1 - e^{-kt^n} \quad (4)$$

where x is the crystallized volume fraction at the time t , n is the Avrami exponent, and k is the reaction rate constant related to the absolute temperature described by the Arrhenius equation:

$$k = k_0 e^{-\frac{E_a}{RT}} \quad (5)$$

where k_0 a constant, E_a is the activation energy, R is the gas constant and T is the absolute temperature.

Table 2 presents results of the activation energy calculated through the three methods, which shows very similar values for any method. The apparent activation energy E_{a1} of amorphous alloys is strongly dependent on the type of the primary phase. The greater the complexity of the primary phase the longer the distance of atom's diffusion, and as a consequence, the higher the value of E_{a1} . The obtained values of E_{a1} are almost three times the value for the self-diffusion of aluminum [39]. For the glassy $\text{Al}_{82}\text{La}_{10}\text{Fe}_4\text{Ni}_4$ alloy melt-spun at 40 ms^{-1} , the crystallization takes place in three overlapping heat events. The activation energies for three main peaks crystallization events are 290, 302 and 298 kJ/mol by Kissinger method and 286, 298 and 295 kJ/mol by Ozawa method [40]. These activation energies values are lower than those of mechanical alloyed $\text{Al}_{82}\text{La}_{10}\text{Fe}_4\text{Ni}_4$ glassy powder, as seen in Table 2. The high values of E_{a1} are related to the stability of the amorphous phase,

which may bring beneficial consequences for the additional hot consolidation of the alloy, so that the amorphous alloy prepared by MA is difficult to crystallize compares to that of melt spinning one.

Table 2. Activation energy (E_a (kJ/mol)) of $\text{Al}_{82}\text{La}_{10}\text{Fe}_4\text{Ni}_4$ amorphous powder for the crystallization stages determined via three methods.

Peak	Methods		
	Kissinger	Ozawa	Augis-Bennett
1	432.33	443.20	437.76
2	456.75	468.25	462.50

The crystallized volume fraction (x) was determined by measuring the corresponding partial area of the exothermic peak. The parameters of the JMA equation can be calculated by plotting $\ln[-\ln(1-x)]$ versus $\ln(1/T)$ with x between the range of 15% to 85% of transformed fractions, the JMA plots at different heating rates are presented in Figure 6. By measuring the slopes of these plots, the values of the Avrami exponents were evaluated and are summarized in Table 3. The average values were 1.41 and 3.61 in the first and the second crystallization process, respectively, as shown in Table 3.

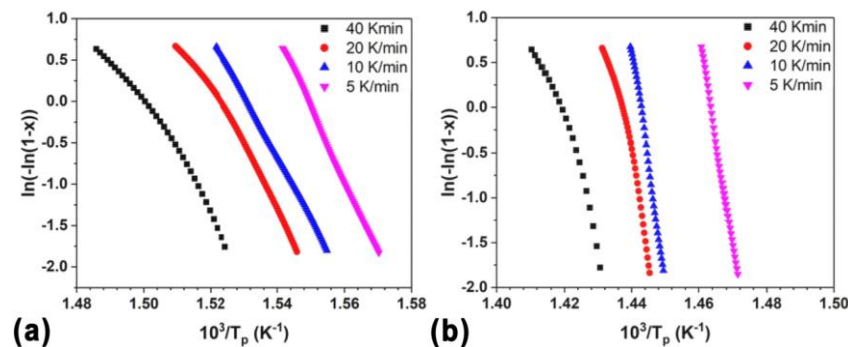


Figure 6. JMA plots for 1st (a) and 2nd (b) crystallization peaks of $\text{Al}_{82}\text{La}_{10}\text{Fe}_4\text{Ni}_4$ amorphous alloys at different heating rates.

Table 3. The Avrami exponent in the first and the second crystallization peaks.

Peak	n	40 K/min	20 K/min	10 K/min	5 K/min
1	1.41	1.16	1.33	1.42	1.71
2	3.61	2.07	3.12	4.84	4.41

It is noteworthy that the anomalously small value of the Avrami exponent is related to some unique features of mechanisms involved in nanocrystals' formation such as the increase in the quenched-in nucleation sites, which accelerates the nucleation rate of the primary phase, blocking the growth process, and giving a quasi-stable grain size.

Average values of n of about 1.41 suggest almost zero nucleation rate [2]. This behavior can be understood by considering the phase formation during crystallization. The first crystallization event is mainly characterized by the formation of fcc-Al mostly through a nucleation and growth mechanism. However, each formed fcc-Al nanocrystal rejects solute elements Ni, Fe, and La into the residual amorphous matrix, thus reducing the driving force for the formation of additional fcc-Al and significantly reducing the nucleation rate, according to the small value of the Avrami exponent ($n = 1.41$). Values of n of about 3.61 confirm the above observation regarding phase transformation when discussing Figure 4. In other words, it may be related to a transformation mechanism characterized by diffusion controlled three-dimensional growth and increasing nucleation rate [41], related to the conversion of fcc-Al into $\text{Al}_{11}\text{La}_3$.

In this section, it was shown that the production of powders of the amorphous $\text{Al}_{82}\text{La}_{10}\text{Fe}_4\text{Ni}_4$ alloy after 350 h of milling in a planetary mill. Such powders had a unimodal distribution and an average particle size of about $14.42\ \mu\text{m}$. After thermal analysis, two exothermic peaks during heating being the first related mainly to the precipitation of fcc-Al, and the second was attributed to phase transformation from fcc-Al to the intermetallic $\text{Al}_{11}\text{La}_3$ phase were observed. The Avrami exponent (n) calculated for the first peak was about 1.41, suggesting almost a zero nucleation rate. Such value was about 3.61 for the second peak, characterizing a diffusion controlled three-dimensional growth and increasing the nucleation rate. Activation energies calculated by three different methods were found to be similar. A high value for the activation energy for the first crystallization was observed, indicating high stability of the amorphous phase.

In the next section, the sintering behavior of the amorphous $\text{Al}_{82}\text{La}_{10}\text{Fe}_4\text{Ni}_4$ powders sintered at different temperatures by SPS to obtain bulks will be analyzed in addition to densification, final microstructural, and structural features, and relate them to mechanical and fracture behaviors.

3.2. Consolidation and Mechanical Properties

The amorphous $\text{Al}_{82}\text{La}_{10}\text{Fe}_4\text{Ni}_4$ powder was consolidated by SPS at temperatures just below the first crystallization event to produce bulk samples with retained amorphous structure. Figure 7a–f illustrates OM images of the polished surface of amorphous $\text{Al}_{82}\text{La}_{10}\text{Fe}_4\text{Ni}_4$ bulk samples sintered at different temperatures between 543 and 623 K, under a pressure of 500 MPa with 3 min of holding time.

Large porosity (dark-gray contrast in Figure 7a) appears clearly throughout the samples sintered at 543 K, whose relative density was measured to be about 88.1%. However, with the increase of the sintering temperature, pores were gradually and rapidly removed such in 563, 583, 603, 613, and 623 K (Figure 7b–f, respectively). The values found for the relative density in the above sequence of temperatures were 95.0, 95.5, 96.0, 96.1, and 97.2% (Figure 8b). In other words, higher densities are obtained at the higher sintering temperature.

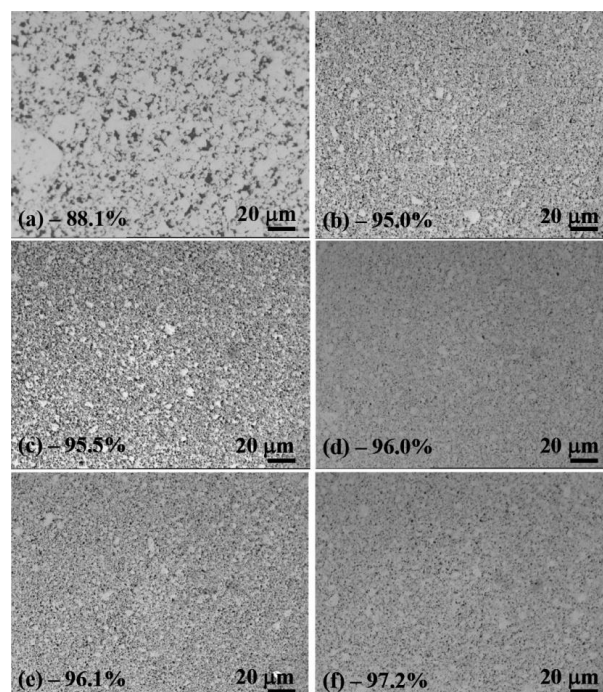


Figure 7. Optical micrographs of polished surface of $\text{Al}_{82}\text{La}_{10}\text{Fe}_4\text{Ni}_4$ bulk samples after spark-plasma sintered at (a) 543, (b) 563, (c) 583, (d) 603, (e) 613, and (f) 623 K.

Figure 8a presents XRD patterns of amorphous powder and sintered samples at various sintering temperatures. Certainly, the amorphous structure is retained at sintering temperatures below 603 K.

Broad peaks correspond to amorphous structures and shift towards higher scattering angle values, from about 36° in the as-milled condition, to 38° at 603 K. The peak shift could be due the release of internal stresses.

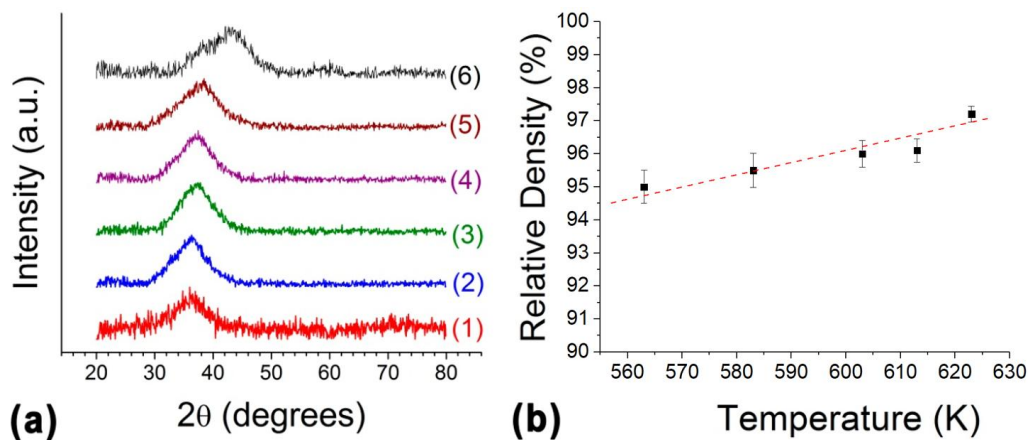


Figure 8. (a) XRD patterns of amorphous $\text{Al}_{82}\text{La}_{10}\text{Fe}_4\text{Ni}_4$ samples: (1) as-milled powder and sintered at SPS at (2) 543, (3) 563, (4) 583, (5) 603 and (6) 623 K, under pressure of 500 MPa, 3 min holding. (b) Relative densities as a function of the SPS temperature.

At the highest sintering temperature of 623 K, the peak shifts to the higher diffraction angle of about 43° . However, clearly, there is a shoulder on the left side of the major peak, corresponding to about 38° , which is the same as for the condition of 603 K. This behavior means that there is a contribution of an amorphous phase and another from a possible nanocrystals' precipitation. Additionally, confirming this last statement is the appearance of a second broad peak on the righter side of the first peak at about 60° and the sudden increase the relative density of the sample sintered at 623 K as shown in Figure 8b, which is the highest at about 97.2%. This relative density value is lower than that of Petersen et al. for amorphous Ni-based alloy (> 99%) due to using the high pressure of 1 GPa and sintering after the first crystallization peak of 948 K together with screened ball-milled powder volume fractions of 60% with diameters $53 \div 106 \mu\text{m}$ and 40% with diameters $< 53 \mu\text{m}$ [42]. Figure 9 presents the results of density and micro-hardness measurements for the bulk amorphous $\text{Al}_{82}\text{La}_{10}\text{Fe}_4\text{Ni}_4$ samples at various sintering temperatures. As for the relative densities, the density of bulk amorphous $\text{Al}_{82}\text{La}_{10}\text{Fe}_4\text{Ni}_4$ samples was strongly dependent on the sintering temperatures, which grows almost linearly with the temperature. The highest density was observed for the sample sintered at approximately 623 K, reaching about $3.29 \text{ g}\cdot\text{cm}^{-3}$, as shown in Figure 9a. In the same sense as for densities, the micro-hardness of bulk samples increased almost linearly with the temperature. The dashed line is a linear fitting considering the instrumental error. In this way, considering such an instrumental error, the highest hardness was also acquired by the sample sintered at 623 K, where the micro-hardness was, on average $\sim 350 \text{ HV}_{0.25}$ (Figure 9b). This behavior may be attributed to the risen densification of the samples, as shown in Figures 7, 8b and 9a.

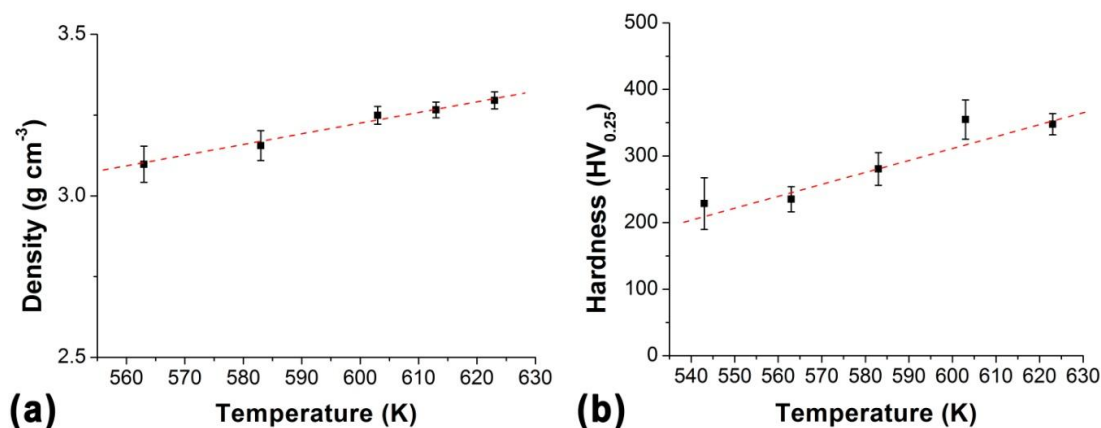


Figure 9. (a) Density and (b) micro-hardness of amorphous $\text{Al}_{82}\text{La}_{10}\text{Fe}_4\text{Ni}_4$ samples at various sintering temperatures.

Figure 10 shows the compressive stress-strain curve for such condition. The fracture strength of the sintered sample reached 650 MPa with a nominal strain of about 2.34%, but without plastic strain before the catastrophic failure. In spite of having strength higher than the hardenable 7XXX series aluminum alloys [43,44], it should be expected greater strength for the amorphous condition. However, as stated above, the condition of 573 K was not fully densified. Thus, porosity played the role by accelerating the failure.

Figure 11 shows FE-SEM images of the $\text{Al}_{82}\text{La}_{10}\text{Fe}_4\text{Ni}_4$ sample sintered at 573 K after the compression test. As stated above, porosity was the main reason behind the failure, as it can be observed in Figure 11a. However, the trans-particle fracture mechanism observed in Figure 11b indicates the efficiency of the sintering condition, which, if fully densified, both strength and strain-to-failure could be even higher.

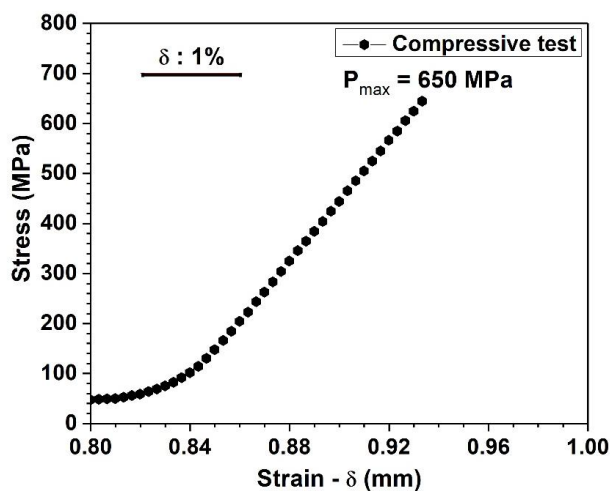


Figure 10. Compression test of sintered samples at 573 K.

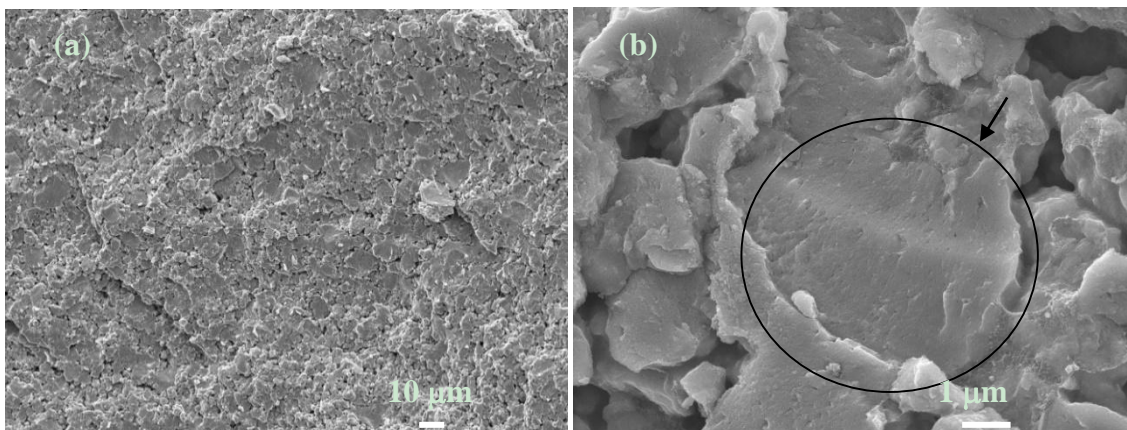


Figure 11. The fracture surface of $\text{Al}_{82}\text{La}_{10}\text{Fe}_4\text{Ni}_4$ compact sintered at 573 K at different magnification of (a) 500 \times and (b) 10,000 \times .

4. Conclusions

Fully amorphous $\text{Al}_{82}\text{La}_{10}\text{Fe}_4\text{Ni}_4$ alloy powder has a unimodal distribution and an average particle size ($d_{0.5}$) of about 14.42 μm obtained after 350 h of milling using a planetary ball mill. Thermal analysis revealed two exothermic peaks during heating. The first is due to crystallization, where mainly fcc-Al is precipitating, and the second was attributed to phase transformation from fcc-Al to the intermetallic $\text{Al}_{11}\text{La}_3$ phase. The precipitation of fcc-Al and intermetallic $\text{Al}_{11}\text{La}_3$ phase progresses with an Avrami exponent (n) for the first peak of about 1.41, suggesting almost a zero nucleation rate. However, the value of n of about 3.61 is related to the phase transformation mechanism, which is characterized by diffusion controlled three-dimensional growth and increasing nucleation rate. The values of activation energies calculated by three different methods are very similar. The high activation energy for the first crystallization indicates mainly the stability of the amorphous state. The sintering behavior of the amorphous $\text{Al}_{82}\text{La}_{10}\text{Fe}_4\text{Ni}_4$ powder alloy shows two maximum in shrinkage rate around 423 and 573 K. After sintering below 603 K, bulk samples retained amorphous structure as seen from XRD patterns. The highest density was observed for sample sintered at approximately 623 K, which was about 3.29 $\text{g}\cdot\text{cm}^{-3}$. The hardness value of compact sample reaches a maximum value of ~ 350 $\text{HV}_{0.25}$ at a sintering temperature of 623 K. The consolidated bulk material exhibits a high compressive strength of 650 MPa with maximum elongation of 2.34%, but without plastic deformation. Porosity was ascertained as being the responsible for this behavior. The morphology of the failure surface of the bulk amorphous $\text{Al}_{82}\text{La}_{10}\text{Fe}_4\text{Ni}_4$ alloy shows the transparticle-fracture mechanism, indicating the efficiency of the sintering condition. Further research in the specific subject of crystallization of bulks and comparison with the results from ribbons will be performed in a future work.

Author Contributions: N.H.V and N.T.H.O. performed research, analyzed the data and wrote the paper; J.-S.K. and A.M.J.J assisted in the data analysis and revised manuscript.

Funding: This research is funded by Vietnam National Foundation for Science and Technology Development (NAFOSTED) under grant number 103.02-2017.366.

Conflicts of Interest: The authors declare no conflict of interest.

References

1. Inoue, A.; Kita, K.; Ohtera, K.; Kimura, H.; Masumoto, T. Al-Y-Ni amorphous powders prepared by high-pressure gas atomization. *J. Mater. Sci. Lett.* **1988**, *7*, 1287–1290. [[CrossRef](#)]
2. Ye, F.; Lu, K. Crystallization kinetics of Al-La-Ni amorphous alloy. *J. Non Cryst. Solids* **2000**, *262*, 228–235. [[CrossRef](#)]

3. Zhang, Z.; Witkin, D.; Lavernia, E.J. Crystallization behavior of a gas atomized $\text{Al}_{85}\text{Ni}_{10}\text{La}_5$ amorphous alloy. *J. Non Cryst. Solids* **2005**, *351*, 1646–1652. [[CrossRef](#)]
4. Scudino, S.; Surreddi, K.B.; Nguyen, H.V.; Liu, G.; Gemming, T.; Sakaliyska, M.; Kim, J.S.; Vierke, J.; Wollgarten, M.; Eckert, J. High-strength $\text{Al}_{87}\text{Ni}_8\text{La}_5$ bulk alloy produced by spark plasma sintering of gas atomized powders. *J. Mater. Res.* **2011**, *24*, 2909–2916. [[CrossRef](#)]
5. Zhuo, L.-C.; Pang, S.-J.; Wang, H.; Zhang, T. Ductile Bulk Aluminum-Based Alloy with Good Glass-Forming Ability and High Strength. *Chin. Phys. Lett.* **2009**, *26*, 066402.
6. Inoue, A.; Matsumoto, N.; Masumoto, T. Al-Ni-Y-Co Amorphous Alloys with High Mechanical Strengths, Wide Supercooled Liquid Region and Large Glass-Forming Capacity. *Mater. Trans. JIM* **1990**, *31*, 493–500. [[CrossRef](#)]
7. Kim, Y.-H.; Inoue, A.; Masumoto, T. Mechanical properties of $\text{Al}_{88}(\text{Y}_{1-x}\text{Ce}_x)_2\text{Ni}_9\text{Fe}_1$ ($x = 0, 0.5, 1$) amorphous alloys containing nanoscale fcc-Al particles. *J. Jpn. Inst. Met.* **1992**, *42*, 217–223. [[CrossRef](#)]
8. Zhong, Z.C.; Jiang, X.Y.; Greer, A.L. Nanocrystallization in Al-based amorphous alloys. *Philos. Mag. B* **1997**, *76*, 505–510. [[CrossRef](#)]
9. Tsai, A.P.; Kamiyama, T.; Kawamura, Y.; Inoue, A.; Masumoto, T. Formation and precipitation mechanism of nanoscale Al particles in Al-Ni base amorphous alloys. *Acta Mater.* **1997**, *45*, 1477–1487. [[CrossRef](#)]
10. Gloriant, T.; Greer, A.L. Al-based nanocrystalline composites by rapid solidification of Al-Ni-Sm alloys. *Nanostruct. Mater.* **1998**, *10*, 389–396. [[CrossRef](#)]
11. Johnson, W.L. Bulk Glass-Forming Metallic Alloys: Science and Technology. *MRS Bull.* **2013**, *24*, 42–56. [[CrossRef](#)]
12. Wang, W.H. Bulk Metallic Glasses with Functional Physical Properties. *Adv. Mater.* **2009**, *21*, 4524–4544. [[CrossRef](#)]
13. Eckert, J.; Das, J.; Pauly, S.; Duhamel, C. Mechanical properties of bulk metallic glasses and composites. *J. Mater. Res.* **2011**, *22*, 285–301. [[CrossRef](#)]
14. Xu, J.; Ramamurty, U.; Ma, E. The fracture toughness of bulk metallic glasses. *JOM* **2010**, *62*, 10–18. [[CrossRef](#)]
15. Suryanarayana, C.; Inoue, A. *Bulk Metallic Glasses*; CRC Press: Boca Raton, FL, USA, 2017.
16. Masumoto, T. Recent progress in amorphous metallic materials in Japan. *Mater. Sci. Eng. A* **1994**, *179–180*, 8–16. [[CrossRef](#)]
17. Peker, A.; Johnson, W.L. A highly processable metallic glass: $\text{Zr}_{41.2}\text{Ti}_{13.8}\text{Cu}_{12.5}\text{Ni}_{10.0}\text{Be}_{22.5}$. *Appl. Phys. Lett.* **1993**, *63*, 2342–2344. [[CrossRef](#)]
18. Schroers, J.; Johnson, W.L. Highly processable bulk metallic glass-forming alloys in the Pt-Co-Ni-Cu-P system. *Appl. Phys. Lett.* **2004**, *84*, 3666–3668. [[CrossRef](#)]
19. Inoue, A.; Zhang, T.; Nishiyama, N.; Ohba, K.; Masumoto, T. Preparation of 16 mm Diameter Rod of Amorphous $\text{Zr}_{65}\text{Al}_{7.5}\text{Ni}_{10}\text{Cu}_{17.5}$ Alloy. *Mater. Trans. JIM* **1993**, *34*, 1234–1237. [[CrossRef](#)]
20. Perepezko, J.H.; Smith, J.S. Glass formation and crystallization in highly undercooled Te-Cu alloys. *J. Non Cryst. Solids* **1981**, *44*, 65–83. [[CrossRef](#)]
21. Si, P.; Bian, X.; Li, W.; Zhang, J.; Yang, Z. Relationship between intermetallic compound formation and glass forming ability of Al-Ni-La alloy. *Phys. Lett. A* **2003**, *319*, 424–428. [[CrossRef](#)]
22. Tavoosi, M.; Karimzadeh, F.; Enayati, M.H.; Kim, H.S. Consolidation of amorphous $\text{Al}_{80}\text{Fe}_{10}\text{Ti}_5\text{Ni}_5$ powders by hot pressing. *J. Nanomater.* **2012**, *2012*. [[CrossRef](#)]
23. Suryanarayana, C. Mechanical alloying and milling. *Prog. Mater. Sci.* **2001**, *46*, 1–184. [[CrossRef](#)]
24. Johnson, W.L. Thermodynamic and kinetic aspects of the crystal to glass transformation in metallic materials. *Prog. Mater. Sci.* **1986**, *30*, 81–134. [[CrossRef](#)]
25. Choi, P.P.; Kim, J.S.; Nguyen, O.T.H.; Kwon, D.H.; Kwon, Y.S.; Kim, J.C. Al-La-Ni-Fe bulk metallic glasses produced by mechanical alloying and spark-plasma sintering. *Mater. Sci. Eng. A* **2007**, *449–451*, 1119–1122. [[CrossRef](#)]
26. Nguyen, V.H.; Nguyen, O.T.H.; Dudina, D.V.; Le, V.V.; Kim, J.-S. Crystallization Kinetics of Al-Fe and Al-Fe-Y Amorphous Alloys Produced by Mechanical Milling. *J. Nanomater.* **2016**, *2016*. [[CrossRef](#)]
27. Schultz, L. Formation of amorphous metals by mechanical alloying. *Mater. Sci. Eng.* **1988**, *97*, 15–23. [[CrossRef](#)]
28. Dudina, D.V.; Mukherjee, A.K. Reactive Spark Plasma Sintering: Successes and Challenges of Nanomaterial Synthesis. *J. Nanomater.* **2013**, *2013*. [[CrossRef](#)]

29. Yurlova, M.S.; Demenyuk, V.D.; Lebedeva, L.Y.; Dudina, D.V.; Grigoryev, E.G.; Olevsky, E.A. Electric pulse consolidation: An alternative to spark plasma sintering. *J. Mater. Sci.* **2014**, *49*, 952–985. [[CrossRef](#)]
30. Kim, S.-Y.; Lee, G.-Y.; Park, G.-H.; Kim, H.-A.; Lee, A.Y.; Scudino, S.; Prashanth, K.G.; Kim, D.-H.; Eckert, J.; Lee, M.-H. High strength nanostructured Al-based alloys through optimized processing of rapidly quenched amorphous precursors. *Sci. Rep.* **2018**, *8*, 1090. [[CrossRef](#)] [[PubMed](#)]
31. Li, X.P.; Yan, M.; Ji, G.; Qian, M. Applied pressure on altering the nano-crystallization behavior of Al₈₆Ni₆Y_{4.5}Co₂La_{1.5} metallic glass powder during spark plasma sintering and its effect on powder consolidation. *J. Nanomater.* **2013**, *2013*. [[CrossRef](#)]
32. Vidyasagar, C.S.; Karunakar, D.B. Development of 2024 AA-Yttrium composites by Spark Plasma Sintering. *IOP Conf. Ser. Mater. Sci. Eng.* **2018**, *346*, 012050. [[CrossRef](#)]
33. Surreddi, K.B.; Srivastava, V.C.; Scudino, S.; Sakaliyska, M.; Uhlenwinkel, V.; Kim, J.S.; Eckert, J. Production of high-strength Al₈₅Y₈Ni₅Co₂ bulk alloy by spark plasma sintering. *J. Phys. Conf. Ser.* **2010**, *240*, 012155. [[CrossRef](#)]
34. Surreddi, K.B.; Scudino, S.; Sakaliyska, M.; Prashanth, K.G.; Sordelet, D.J.; Eckert, J. Crystallization behavior and consolidation of gas-atomized Al₈₄Gd₆Ni₇Co₃ glassy powder. *J. Alloys Compd.* **2010**, *491*, 137–142. [[CrossRef](#)]
35. Heireche, L.; Belhadji, M. The methods Matusita, Kissinger and Ozawa in the study of the crystallization of glasses. The case of Ge-Sb-Te alloys. *Chalcogenide Lett.* **2007**, *4*, 23–33.
36. Mehta, N.; Agarwal, P.; Kumar, A. A study of the crystallization kinetics in Se₆₈Ge₂₂Pb₁₀ chalcogenide glass. *Indian J. Eng. Mater. Sci.* **2004**, *11*, 511–515.
37. Roy, D.; Raghuvanshi, H. Study on crystallization kinetics of Al₆₅Cu₂₀Ti₁₅ amorphous alloy. *J. Non Cryst. Solids* **2011**, *357*, 1701–1704. [[CrossRef](#)]
38. Sahoo, K.L.; Rao, V.; Mitra, A. Crystallization Kinetics in an Amorphous Al-Ni-Mm-Fe Alloy. *Mater. Trans.* **2003**, *44*, 1075–1080. [[CrossRef](#)]
39. Wang, X.; Wang, D.; Zhu, B.; Li, Y.; Han, F. Crystallization kinetics and thermal stability of mechanically alloyed Al₇₆Ni₈Ti₈Zr₄Y₄ glassy powder. *J. Non Cryst. Solids* **2014**, *385*, 111–116. [[CrossRef](#)]
40. Basu, J.; Ranganathan, S. Crystallisation in Al-ETM-LTM-La metallic glasses. *Intermetallics* **2004**, *12*, 1045–1050. [[CrossRef](#)]
41. Mohammadi Rahvard, M.; Tamizifar, M.; Boutorabi, S.M.A. Non-isothermal crystallization kinetics and fragility of Zr₅₆Co₂₈Al₁₆ and Zr₅₆Co₂₂Cu₆Al₁₆ bulk metallic glasses. *J. Therm. Anal. Calorim.* **2018**. [[CrossRef](#)]
42. Petersen, A.S.; Cheung, A.M.; Neilson, H.J.; Poon, S.J.; Shiflet, G.J.; Lewandowski, J.J. Processing and Properties of Ni-Based Bulk Metallic Glass via Spark Plasma Sintering of Pulverized Amorphous Ribbons. *MRS Adv.* **2017**, *2*, 3815–3820. [[CrossRef](#)]
43. Rometsch, P.A.; Zhang, Y.; Knight, S. Heat treatment of 7xxx series aluminium alloys—Some recent developments. *Trans. Nonferrous Met. Soc. China* **2014**, *24*, 2003–2017. [[CrossRef](#)]
44. Sheng, X.; Lei, Q.; Xiao, Z.; Wang, M. Hot Deformation Behavior of a Spray-Deposited Al-8.31Zn-2.07Mg-2.46Cu-0.12Zr Alloy. *Metals* **2017**, *7*, 299. [[CrossRef](#)]

